

# Instabilities near ultrastrong coupling in microwave optomechanical cavity

Soumya Ranjan Das,<sup>1</sup> Sourav Majumder,<sup>1</sup> Sudhir Kumar Sahu,<sup>1</sup>  
Ujjawal Singhal,<sup>1</sup> Tanmoy Bera,<sup>1</sup> and Vibhor Singh<sup>1,\*</sup>

<sup>1</sup>*Department of Physics, Indian Institute of Science, Bangalore-560012 (India)*

(Dated: August 21, 2023)

With artificially engineered systems, it is now possible to realize the coherent interaction rate, which can become comparable to the mode frequencies, a regime known as ultrastrong coupling (USC). We experimentally realize a cavity-electromechanical device using a superconducting waveguide cavity and a mechanical resonator. In the presence of a strong pump, the mechanical-polaritons splitting can nearly reach 81% of the mechanical frequency, overwhelming all the dissipation rates. Approaching the USC limit, the steady-state response becomes unstable. We systematically measure the boundary of the unstable response while varying the pump parameters. The unstable dynamics display rich phases, such as self-induced oscillations, period-doubling bifurcation, period-tripling oscillations, and ultimately leading to the chaotic behavior. The experimental results and their theoretical modeling suggest the importance of residual nonlinear interaction terms in the weak-dissipative regime.

Keywords: Cavity optomechanics, Ultrastrong coupling, Route to chaos, Parametric instability

## I. INTRODUCTION:

Radiation-pressure interaction is fundamental to the cavity-optomechanical systems consisting of a mechanical mode coupled to an electromagnetic mode (EM) [1]. With technological advancements, cavity optomechanical devices have been successful in controlling the low-frequency mechanical mode down to their quantum regime [2]. Several demonstrations pertaining to the quantum state preparation [3–6] and entanglement [7–10], signal transduction [11–13], and topological physics using the mechanical modes have been shown [14, 15].

The coherent coupling rate, characterizing the interaction between the EM mode ( $\omega_c$ ) and the mechanical mode ( $\omega_m$ ), is a key figure of merit in such devices [1, 2]. The energy dissipation rates of the two modes ( $\kappa, \gamma_m$ ) capture the incoherent coupling with their thermal baths. Based on the relative strengths of these rates, several interesting scenarios are feasible. When the coherent coupling rate ( $g$ ) exceeds the dissipative coupling rates of the two modes ( $g \gg \kappa, \gamma_m$ ), the two modes hybridize, resulting in new eigenstates [16, 17]. Further, when the coherent coupling rate becomes a significant fraction of the mode frequencies, the composite system enters the “ultrastrong coupling” (USC) limit [18]. In this limit, the two modes hybridize in a non-trivial way leading to an entangled ground state in the quantum regime [19, 20]. The USC limit has been experimentally demonstrated in several systems where two modes interact nearly resonantly [21, 22].

In cavity optomechanical systems, however, the EM mode and mechanical mode interact dispersively ( $\omega_c \gg \omega_m$ ). The nonlinear radiation-pressure interaction can be described by  $H_i/\hbar = -g_0 a^\dagger a(b + b^\dagger)$ , where  $g_0$  is the single-photon coupling strength and  $a(b)$ 's are the ladder

operators for the cavity(mechanical) mode. In the presence of a strong coherent pump, the interaction Hamiltonian can be linearized to  $H_i/\hbar \simeq -g(a + a^\dagger)(b + b^\dagger)$ , where  $g = g_0 \sqrt{n_d}$  is the parametric coupling rate and  $n_d$  is the number of the pump photons in the cavity. With the ability to control the parametric coupling rate, several regimes, such as quantum coherent coupling, and steady-state quantum entanglement between the two modes can be reached [10, 17, 23]. Ultimately, owing to the nonlinear nature of the radiation-pressure interaction, the response becomes unstable, as shown schematically in Fig. 1.

Indeed, various phenomena in the unstable region such as limit cycle, period doubling bifurcations, and chaos have been extensively studied [24–28]. Experimentally, these effects have been primarily explored in the strong dissipative regime ( $\omega_m \lesssim \kappa$ ) or with the blue-detuned pump [29–35] (see Fig. 1). The instabilities near the ultrastrong coupling limit, however, allow to explore the nonlinear dynamics of the cavity optomechanical system in the *weakly dissipative* limit ( $\gamma_m, \kappa \ll 2g \lesssim \omega_m$ ). The nonlinear dynamics with weak dissipation is unique and is predicted to show transient chaos, quasi-periodic route to chaos and lower threshold powers for the onset of chaos [36, 37].

Here, we use a cavity electromechanical device in the microwave domain to probe the route to chaos when it is operated into the USC limit. We first demonstrate the USC by performing the spectroscopic and time-domain measurements. We probe the stability of the device when the pump detuning near the red sideband and injected power are varied. The unstable region shows very rich phases in the parameter space, such as the self-induced oscillation, period-doubling bifurcations, period-tripling oscillations, and chaotic behavior [26, 36, 37]. We find that the measured threshold powers for the onset of instabilities are lower than the ones predicted from a nonlinear model considering the optomechanical interaction

\* v.singh@iisc.ac.in

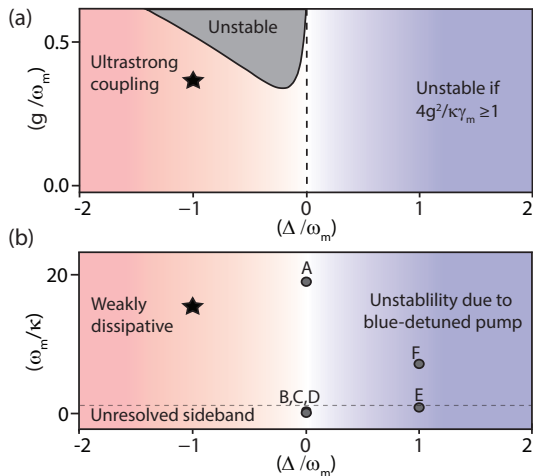


FIG. 1. (a) The schematic of the parameter space of a cavity-electromechanical system in the steady state marking the USC regime and the region of unstable response. This study has been marked by  $\star$ . (b) comparison the sideband-resolution parameter of this study and the earlier studies on instabilities. The data points A to F are from refs [30–35], respectively. The symbols  $g$ ,  $\omega_m$ ,  $\kappa$ , and  $\Delta$  represent the optomechanical coupling strength, the mechanical frequency, cavity dissipation rate, and the pump detuning from the cavity resonant frequency, respectively.

and a Kerr-term in the cavity.

## II. EXPERIMENTAL DETAILS:

We use the three-dimensional cavity-based platform to realize the cavity-electromechanical device [38–40]. The waveguide cavity-based electromechanical device offers a higher dynamic range for the pumped photons, which is highly desirable to reach the USC limit [40, 41]. As shown in Fig. 2(a) and 2(b), the device consists of a rectangular waveguide cavity, and a drumhead-shaped mechanical resonator in the form of a parallel plate capacitor patterned on a sapphire chip. The patterned sapphire chip fabricated with aluminum is placed at the center of the cavity. The electrical pads to the drumhead are then directly wire-bonded to the cavity walls to integrate with the cavity mode [40].

The sample-mounted cavity is cooled down to 20 mK in a dilution fridge. Fig. 2(c) shows the measurement of the cavity transmission at the base temperature. The bare cavity is designed to have the fundamental resonant mode frequency of 7.5 GHz. However, the electromechanical capacitor perturbs the mode shape significantly, and lowers the mode frequency to  $\omega_c/2\pi \approx 4.86$  GHz. The reduction in the resonant frequency of the cavity results from the electromechanical capacitance and the inductance of the connecting electrodes introduced after the addition of a patterned sapphire chip. We

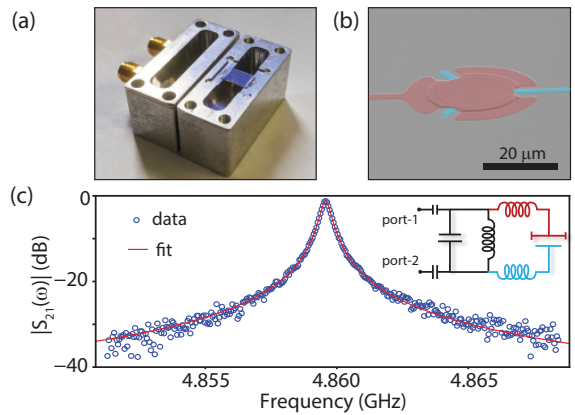


FIG. 2. (a) Image of the waveguide cavity along with a patterned substrate. The cavity has dimensions of  $26 \times 26 \times 6$  mm<sup>3</sup>. (b) False color image of the mechanical resonator forming a parallel plate capacitor with another plate on the substrate. The separation between the capacitor plates at room temperature is approximately 200 nm. (c) Measurement of the voltage transmission coefficient  $|S_{21}|$  of the device at the base temperature. The inset shows the equivalent circuit diagram of the cavity electromechanical device.

measure the input, output, and the internal dissipation rates of  $\kappa_{e1}/2\pi \approx 90$  kHz,  $\kappa_{e2}/2\pi \approx 190$  kHz, and  $\kappa_i/2\pi \approx 100$  kHz, respectively. At low temperatures, we estimated that the gap between the electromechanical capacitor plates reduces to approximately 32 nm due to thermal contraction [42, 43], which helps in achieving a single photon coupling rate  $g_0/2\pi$  of 165 Hz.

## III. ULTRA-STRONG COUPLING REGIME

We measure the transmission coefficient  $|S_{21}(\omega)|$  through the cavity using a weak probe tone while injecting a pump detuned near the red sideband  $\omega_c - \omega_m$ . At relatively lower pump powers, the optomechanically induced absorption setup allows us to determine the mechanical frequency  $\omega_m/2\pi \approx 6.32$  MHz [44]. At relatively higher pump powers, the response turns into two well-separated peaks confirming the new eigenmodes of the system as shown in Fig. 3(a). The peak separation being  $0.81\omega_m$  marks the ultrastrong coupling between the mechanical resonator and the cavity. The transmission measurement shows the presence of an additional weakly coupled mechanical mode, indicated by the red arrow. Two more features arising from the interference of the down-scattered pump signal and the probe signal can be seen. Figure 3(b) shows the measurement of  $|S_{21}|$  as the frequency of the pump is varied while maintaining a constant power at the signal generator.

The presence of a strong intracavity pump field leads to a static shift of the equilibrium position of the mechanical resonator, given by  $x_s = (2g_0n_d/\omega_m)x_{zp}$ , where  $x_{zp}$  is the zero-point motion of the mechanical resonator.

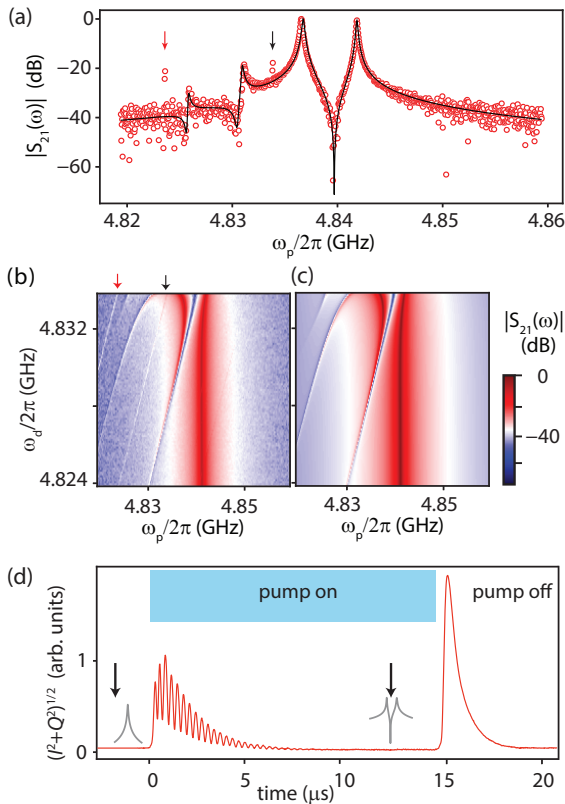


FIG. 3. (a) The normalized magnitude of the cavity transmission  $|S_{21}(\omega)|$  (red-circles) while applying a strong pump near the red sideband. The black line shows the calculated  $|S_{21}(\omega)|$  while including the static Kerr shift of the cavity. (b) The colorplot of measured  $|S_{21}(\omega)|$  as the pump frequency  $\omega_d$  is varied at a fixed pump power of -31 dBm at the cavity. The black arrow shows the position of the pump signal, while the red arrow indicates another weakly coupled mechanical mode. A weak probe signal -88 dBm at the cavity is used to generate the colorplot. (c) Colorplot of  $|S_{21}(\omega)|$  obtained from the calculations. (d) Measurement of the amplitude of the transmitted probe signal in the time domain while modulating the interaction strength. The pump frequency is set near the lower mechanical sideband. The position of the probe signal is schematically represented by the black arrows relative to the steady-state cavity transmission curves (shown in gray).

The shift in the equilibrium position of the mechanical resonator leads to a Kerr shift of the cavity frequency by  $-2g_0^2 n_d / \omega_m$ . The total shift in the cavity frequency comes from the static nature of the radiation-pressure force and nonlinear kinetic inductance of the superconducting aluminum film. We emphasize here that at high pump powers, the Kerr shift of the cavity becomes significant, and it must be considered to capture the cavity transmission faithfully. In this case, we found a cavity shift of  $\sim 1.76$  MHz at the maximum pump power used in the experiment. It corresponds to an optomechanical Kerr coefficient of 8.6 mHz/photon and a kinetic induc-

ance Kerr coefficient of approximately 5 mHz/photon at the maximum pump power (see the Supplemental Material[45]).

To theoretically model the cavity transmission, we expand the interaction Hamiltonian  $H_i$  around the mean field of the pump and obtain the quantum-Langevin equations of motion. Without using the rotating-wave approximation and by retaining the static Kerr shift of the cavity frequency, the steady-state response can be obtained from the inverse of the mode-coupling matrix (see the Supplemental Material[45]). The solid line in Fig. 3(a) and colorplot in Fig. 3(c) show the calculated transmission coefficient using the experimentally determined device parameters. While in general, additional weakly coupled mechanical modes can also be included in the calculations, we neglect them here for simplicity.

The onset of the strong coupling allows for a coherent swap of the excitations between the cavity and the mechanical mode. It thus enables the high-speed optomechanical swap gates in the ultrastrong coupling limit. To explore the maximum speed of the optomechanical swap, we perform time domain measurements in this limit. We modulate the interaction strength  $g(t)$ , which is controlled by the amplitude of the pump tone. The transmission through the cavity is monitored by applying a weak continuous probe signal near  $\omega_c$ . To demodulate the probe signal, we first mix it down using an external mixer and then sending it to a high-speed lock-in amplifier to further demodulate the quadratures with a short integration time (100 ns) (see the Supplemental Material[45]).

Fig. 3(d) shows the measurement of the magnitude of the demodulated signals  $(I(t), Q(t))$  as the interaction strength  $g(t)$  is modulated. For this measurement, the interaction strength is modulated to 1.55 MHz. The probe frequency is detuned from the cavity resonant frequency by  $(\omega_p - \omega_c)/2\pi = 372$  kHz. Therefore, the transmission is small even when the pump tone is off ( $t < 0$ ). In the steady-state when the pump is turned on ( $t \approx 10 \mu\text{s}$ ), the transmission is low again due to the formation of mechanical-polariton modes. Because of the strong static Kerr shift of the cavity, the probe tone appears near the center of the split peaks, resulting in low transmission.

When interaction is just switched on, the transient response shows the oscillations arising from the coherent energy exchange between the mechanical and the cavity modes. The oscillation frequency of 3.1 MHz corresponds to the characteristic swap time of 160 ns. The amplitude of the oscillations decays at a rate  $\simeq \kappa/4$  set by joint dissipation of the two polaritons. When the pump is turned off, the energy stored in the two polariton modes remerges near the probe frequency, and the amplitude decays at  $\kappa/2$ . It is important to remark that as we operate close to the USC limit, the modulated pump signal spectrally overlaps with the probe signal and adds a small offset in the measurement. Additional datasets are provided in the Supplemental Material[45].

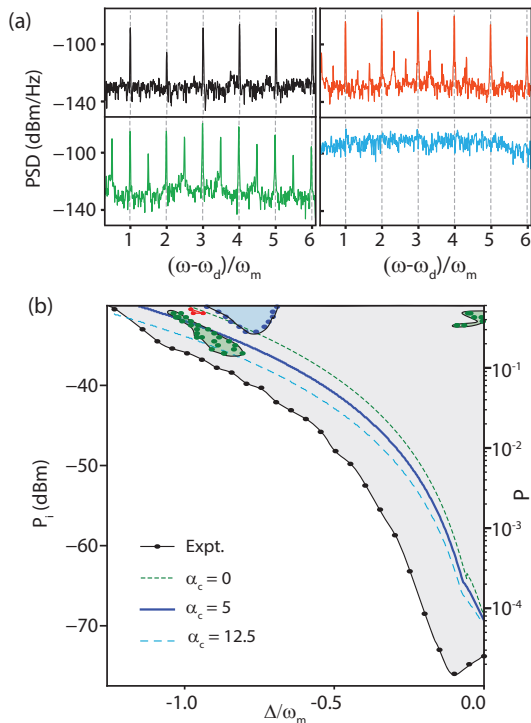


FIG. 4. (a) Measurement of the single sideband microwave power spectral density (PSD) for different injected pump powers  $P_i$ . Different panels show the self-induced oscillations (black), first period-doubling bifurcations (green), period tripling oscillations (red), and the chaotic behavior (blue). (b) The gray region represents the boundary of self-induced oscillations. The black circles are the experimentally measured points. At higher injected pump powers, the region of period-doubling bifurcations is represented by the green region. The period tripling oscillations are shown by the red-colored region. The region of chaotic behavior is shown by the cyan-colored region. Experimentally measured points are shown by the circles of different colors. The solid blue line and the dashed lines show the unstable boundary obtained from the theoretical calculation.

#### IV. PARAMETRIC INSTABILITIES NEAR ULTRA-STRONG COUPLING

After establishing the USC in the present experiment, we now discuss the parametric instabilities arising at the high pump powers. At the core of it, the instabilities stem from the nonlinear interaction between the microwave field and the mechanical motion. To experimentally investigate the phase space of the parametric instabilities and their nature, we measure the microwave power spectral density (PSD) using a spectrum analyzer while varying the pump power  $P_i$  and pump detuning  $\Delta = (\omega_d - \omega_c)$ . As  $P_i$  is increased, the self-induced oscillations appear as multiple peaks separated by  $\omega_m$  in the microwave PSD. Fig. 4(a) shows the PSD of different kinds of responses. The top-left panel corre-

sponds to the instability due to the self-induced oscillations where the peaks are separated by  $\omega_m$ . The bottom-left panel corresponds to the first period-doubling bifurcations (PDB), where the peaks are separated by  $\omega_m/2$ . The top-right panel shows the period-tripled oscillations where the peaks are separated by  $\omega_m/3$ . The bottom-right panel shows the response where the power is uniformly distributed over a broad range of frequencies. It corresponds to the chaotic vibration of the mechanical oscillator undergoing aperiodic oscillations leading to a continuous power spectrum in the output microwave field. These different phases of unstable response are summarized in Fig. 4(b). The gray-color region represents the parametrically unstable response. The boundary of the gray region marks the threshold power for the self-induced oscillations. With decrease in  $\Delta$ , the circulating power in the cavity decreases, and the threshold power for the onset of the instability increases. The regions of first PDB, period tripling oscillations and chaos are color-coded within the unstable region. A discussion on the measurement methodology is included in the Supplemental Material[45].

To understand these results, we use the classical nonlinear dynamics approach. We start with the full cavity optomechanical Hamiltonian *i.e.*  $H_i/\hbar = -g_0\hat{a}^\dagger\hat{a}(\hat{b} + \hat{b}^\dagger)$ . In addition, motivated by the observation of period-tripling oscillations and the relevance of the kinetic inductance at the high pump powers, we include a weak nonlinear term in the cavity Hamiltonian, given by  $-(\alpha_c/2)(\hat{a}^\dagger\hat{a})^2$ . Using the semi-classical approximation, we obtain the classical equations of motion (EOM) for the cavity and the mechanical quadratures. From EOMs, we find the fixed points and perform a linear stability test, which is similar to the Routh-Hurwitz criteria, *i.e.* the solutions are stable if and only if all the eigenvalues of the evolution matrix of small perturbations around the fixed points have a negative real part [46]. Calculation details are provided in the Supplemental Material[45].

Results of these calculations in different limits are shown in Fig. 4(b). We also include a dimensionless power  $P = 8g_0^2n_0/\omega_m^4$  on the right y-axis, where  $n_0$  is defined as the number of photons when the pump is set at the cavity frequency [26, 37]. Clearly, the threshold power estimated from the calculations is larger than the one measured in the experiment. For comparison, the instability boundary obtained while considering the optomechanical Kerr nonlinearity alone ( $\alpha_c = 0$ ), and two non-zero values of  $\alpha_c/2\pi = 5, 12.5$  mHz/photon are also included. We note that even a significantly higher value of  $\alpha_c$  does not fully explain the experimental findings suggesting a different origin. Thus, the nonlinearities arising from the optomechanical interaction and the kinetic inductance do not completely capture the threshold for the unstable region when a linear stability test is applied.

In addition, the numerical calculations do not show the period-doubling bifurcations or chaotic behavior for the pump parameters used in the experiment. In numerical calculations, these effects appear at higher powers than

the ones observed in the experiment. It thus provides the first experimental evidence that the route to chaos in the USC limit or equivalently in the weakly dissipative limit is different from the previously studied cases. It suggests that the role of thermal fluctuations, and residual weak nonlinear coupling terms might be relevant in determining the boundary of the unstable region [47, 48]. In particular, during the transitions from self-oscillation to period-doubling oscillation and subsequently to chaotic regions, the mechanical mode remains in a high amplitude state. In this case, the role of mechanical Duffing nonlinearity, and resonantly-induced negative dissipation might become important [49].

## V. OUTLOOK AND CONCLUSION

In conclusion, we have demonstrated the ultrastrong coupling using a superconducting waveguide cavity and a mechanical resonator, where the splitting of the mechanical polaritons becomes nearly 81% of the mechanical frequency. In the time-domain, we measure optomechanical swap time of 160 ns, which is nearly 16 times shorter than the shortest dissipation time in the device. With suitable modification to the thermalization of the microwave signals, the cavity can be operated in the quantum limit. It would enable a wide variety of experiments such as the entangled ground state properties of the cavity and the mechanical resonator [22], and high speed optome-

chanical gates [43]. Using the pump in a pulse mode, the parametric coupling can be pushed beyond the USC regime [20, 50]. In addition, the microwave frequency comb generated using the optomechanical-nonlinearity can be a valuable resource for sensing applications [36]. The experiment here, for the first time, explores the unstable response in the steady-state in the weakly dissipative limit [37]. Clearly, the theoretical model based on optomechanical and kinetic inductance nonlinearity does not account for the lower threshold powers observed in the experiment. It thus opens up the possibility of further exploring the role of quantum fluctuations [26], and other weak residual couplings in the interaction Hamiltonian [47].

## ACKNOWLEDGMENTS

The authors thank G. S. Agarwal, Manas Kulkarni, and Tamoghana Ray for their valuable discussions. This material is based upon work supported by the Air Force Office of Scientific Research under award No. FA2386-20-1-4003. V.S. acknowledge the support received under the Core Research Grant by the Department of Science and Technology (India). The authors acknowledge device fabrication facilities at CeNSE, IISc Bangalore, and central facilities at the Department of Physics funded by DST (Govt. of India).

- 
- [1] M. Aspelmeyer, T. J. Kippenberg, and F. Marquardt, Cavity optomechanics, *Reviews of Modern Physics* **86**, 1391 (2014).
  - [2] S. Barzanjeh, A. Xuereb, S. Gröblacher, M. Paternostro, C. A. Regal, and E. M. Weig, Optomechanics for quantum technologies, *Nature Physics* **18**, 15 (2022).
  - [3] J. D. Teufel, T. Donner, D. Li, J. W. Harlow, M. S. Allman, K. Cicak, A. J. Sirois, J. D. Whittaker, K. W. Lehnert, and R. W. Simmonds, Sideband cooling of micromechanical motion to the quantum ground state, *Nature* **475**, 359 (2011).
  - [4] J. Chan, T. P. M. Alegre, A. H. Safavi-Naeini, J. T. Hill, A. Krause, S. Gröblacher, M. Aspelmeyer, and O. Painter, Laser cooling of a nanomechanical oscillator into its quantum ground state, *Nature* **478**, 89 (2011).
  - [5] E. A. Wollack, A. Y. Cleland, R. G. Gruenke, Z. Wang, P. Arrangoiz-Arriola, and A. H. Safavi-Naeini, Quantum state preparation and tomography of entangled mechanical resonators, *Nature* **604**, 463 (2022).
  - [6] M. Bild, M. Fadel, Y. Yang, U. von Lüpke, P. Martin, A. Bruno, and Y. Chu, Schrödinger cat states of a 16-microgram mechanical oscillator, arXiv:2211.00449 (2022).
  - [7] T. A. Palomaki, J. W. Harlow, J. D. Teufel, R. W. Simmonds, and K. W. Lehnert, Coherent state transfer between itinerant microwave fields and a mechanical oscillator, *Nature* **495**, 210 (2013).
  - [8] R. Riedinger, A. Wallucks, I. Marinković, C. Löschnauer, M. Aspelmeyer, S. Hong, and S. Gröblacher, Remote quantum entanglement between two micromechanical oscillators, *Nature* **556**, 473 (2018).
  - [9] C. F. Ockeloen-Korppi, E. Damskäg, J.-M. Pirkkalainen, M. Asjad, A. A. Clerk, F. Massel, M. J. Woolley, and M. A. Sillanpää, Stabilized entanglement of massive mechanical oscillators, *Nature* **556**, 478 (2018).
  - [10] S. Kotler, G. A. Peterson, E. Shojaei, F. Lecocq, K. Cicak, A. Kwiatkowski, S. Geller, S. Glancy, E. Knill, R. W. Simmonds, J. Aumentado, and J. D. Teufel, Direct observation of deterministic macroscopic entanglement, *Science* **372**, 622 (2021).
  - [11] R. W. Andrews, R. W. Peterson, T. P. Purdy, K. Cicak, R. W. Simmonds, C. A. Regal, and K. W. Lehnert, Bidirectional and efficient conversion between microwave and optical light, *Nature Physics* **10**, 321 (2014).
  - [12] M. Forsch, R. Stockill, A. Wallucks, I. Marinković, C. Gärtner, R. A. Norte, F. van Otten, A. Fiore, K. Srinivasan, and S. Gröblacher, Microwave-to-optics conversion using a mechanical oscillator in its quantum ground state, *Nature Physics* **16**, 69 (2020).
  - [13] M. Mirhosseini, A. Sipahigil, M. Kalaei, and O. Painter, Superconducting qubit to optical photon transduction, *Nature* **588**, 599 (2020).
  - [14] J. Cha, K. W. Kim, and C. Daraio, Experimental realization of on-chip topological nanoelectromechanical meta-

- materials, *Nature* **564**, 229 (2018).
- [15] A. Youssefi, S. Kono, A. Bancora, M. Chegnizadeh, J. Pan, T. Vovk, and T. J. Kippenberg, Topological lattices realized in superconducting circuit optomechanics, *Nature* **612**, 666 (2022).
- [16] J. D. Teufel, D. Li, M. S. Allman, K. Cicak, A. J. Sirois, J. D. Whittaker, and R. W. Simmonds, Circuit cavity electromechanics in the strong-coupling regime, *Nature* **471**, 204 (2011).
- [17] E. Verhagen, S. Deléglise, S. Weis, A. Schliesser, and T. J. Kippenberg, Quantum-coherent coupling of a mechanical oscillator to an optical cavity mode, *Nature* **482**, 63 (2012).
- [18] C. Ciuti and I. Carusotto, Input-output theory of cavities in the ultrastrong coupling regime: The case of time-independent cavity parameters, *Physical Review A* **74**, 033811 (2006).
- [19] C. Ciuti, G. Bastard, and I. Carusotto, Quantum vacuum properties of the intersubband cavity polariton field, *Physical Review B* **72**, 115303 (2005).
- [20] S. G. Hofer, W. Wiczorek, M. Aspelmeyer, and K. Hammerer, Quantum entanglement and teleportation in pulsed cavity optomechanics, *Physical Review A* **84**, 052327 (2011).
- [21] P. Forn-Díaz, L. Lamata, E. Rico, J. Kono, and E. Solano, Ultrastrong coupling regimes of light-matter interaction, *Reviews of Modern Physics* **91**, 025005 (2019).
- [22] A. F. Kockum, A. Miranowicz, S. D. Liberato, S. Savasta, and F. Nori, Ultrastrong coupling between light and matter, *Nature Reviews Physics* **1**, 19 (2019).
- [23] S. G. Hofer and K. Hammerer, Entanglement-enhanced time-continuous quantum control in optomechanics, *Physical Review A* **91**, 033822 (2015).
- [24] F. Marquardt, J. G. E. Harris, and S. M. Girvin, Dynamical Multistability Induced by Radiation Pressure in High-Finesse Micromechanical Optical Cavities, *Physical Review Letters* **96**, 103901 (2006).
- [25] N. Lörch, J. Qian, A. Clerk, F. Marquardt, and K. Hammerer, Laser Theory for Optomechanics: Limit Cycles in the Quantum Regime, *Physical Review X* **4**, 011015 (2014).
- [26] L. Bakemeier, A. Alvermann, and H. Fehske, Route to Chaos in Optomechanics, *Physical Review Letters* **114**, 013601 (2015).
- [27] C. Schulz, A. Alvermann, L. Bakemeier, and H. Fehske, Optomechanical multistability in the quantum regime, *Europhysics Letters* **113**, 64002 (2016).
- [28] P. Djourwe, Y. Pennec, and B. Djafari-Rouhani, Frequency locking and controllable chaos through exceptional points in optomechanics, *Physical Review E* **98**, 032201 (2018).
- [29] T. J. Kippenberg, H. Rokhsari, T. Carmon, A. Scherer, and K. J. Vahala, Analysis of Radiation-Pressure Induced Mechanical Oscillation of an Optical Microcavity, *Physical Review Letters* **95**, 033901 (2005).
- [30] T. Carmon, M. C. Cross, and K. J. Vahala, Chaotic Quivering of Micron-Scaled On-Chip Resonators Excited by Centrifugal Optical Pressure, *Physical Review Letters* **98**, 167203 (2007).
- [31] F. M. Buters, H. J. Eerkins, K. Heeck, M. J. Weaver, B. Pepper, S. de Man, and D. Bouwmeester, Experimental exploration of the optomechanical attractor diagram and its dynamics, *Physical Review A* **92**, 013811 (2015).
- [32] F. Monifi, J. Zhang, a. K. Özdemir, B. Peng, Y.-x. Liu, F. Bo, F. Nori, and L. Yang, Optomechanically induced stochastic resonance and chaos transfer between optical fields, *Nature Photonics* **10**, 399 (2016).
- [33] D. Navarro-Urrios, N. E. Capuj, M. F. Colombano, P. D. García, M. Sledzinska, F. Alzina, A. Griol, A. Martínez, and C. M. Sotomayor-Torres, Nonlinear dynamics and chaos in an optomechanical beam, *Nature Communications* **8**, 14965 (2017).
- [34] R. Leijssen, G. R. La Gala, L. Freisem, J. T. Muhonen, and E. Verhagen, Nonlinear cavity optomechanics with nanomechanical thermal fluctuations, *Nature Communications* **8**, ncomms16024 (2017).
- [35] J. Shin, Y. Ryu, M.-A. Miri, S.-B. Shim, H. Choi, A. Alù, J. Suh, and J. Cha, On-Chip Microwave Frequency Combs in a Superconducting Nanoelectromechanical Device, *Nano Letters* **22**, 5459 (2022).
- [36] M.-A. Miri, G. D’Aguanno, and A. Alù, Optomechanical frequency combs, *New Journal of Physics* **20**, 043013 (2018).
- [37] T. F. Roque, F. Marquardt, and O. M. Yevtushenko, Nonlinear dynamics of weakly dissipative optomechanical systems, *New Journal of Physics* **22**, 013049 (2020).
- [38] M. Yuan, V. Singh, Y. M. Blanter, and G. A. Steele, Large cooperativity and microkelvin cooling with a three-dimensional optomechanical cavity, *Nature Communications* **6**, 8491 (2015).
- [39] A. Noguchi, R. Yamazaki, M. Ataka, H. Fujita, Y. Tabuchi, T. Ishikawa, Koji Usami, and Y. Nakamura, Ground state cooling of a quantum electromechanical system with a silicon nitride membrane in a 3D loop-gap cavity, *New Journal of Physics* **18**, 103036 (2016).
- [40] B. Gunupudi, S. R. Das, R. Navarathna, S. K. Sahu, S. Majumder, and V. Singh, Optomechanical Platform with a Three-dimensional Waveguide Cavity, *Physical Review Applied* **11**, 024067 (2019).
- [41] G. Peterson, S. Kotler, F. Lecocq, K. Cicak, X. Jin, R. Simmonds, J. Aumentado, and J. Teufel, Ultrastrong Parametric Coupling between a Superconducting Cavity and a Mechanical Resonator, *Physical Review Letters* **123**, 247701 (2019).
- [42] E. E. Wollman, C. U. Lei, A. J. Weinstein, J. Suh, A. Kronwald, F. Marquardt, A. A. Clerk, and K. C. Schwab, Quantum squeezing of motion in a mechanical resonator, *Science* **349**, 952 (2015).
- [43] A. P. Reed, K. H. Mayer, J. D. Teufel, L. D. Burkhardt, W. Pfaff, M. Reagor, L. Sletten, X. Ma, R. J. Schoelkopf, E. Knill, and K. W. Lehnert, Faithful conversion of propagating quantum information to mechanical motion, *Nature Physics* **13**, 1163 (2017).
- [44] S. Weis, R. Rivière, S. Deléglise, E. Gavartin, O. Arcizet, A. Schliesser, and T. J. Kippenberg, Optomechanically Induced Transparency, *Science* **330**, 1520 (2010).
- [45] See supplemental material at [url will be inserted by publisher] for additional experimental results and the theoretical calculations. it includes two additional references [51, 52].
- [46] I. S. Gradshteyn and I. M. Ryzhik, *Table of Integrals, Series, and Products*, 7th ed. (Academic Press, Amsterdam, 2007).
- [47] M. A. Lemonde, N. Didier, and A. A. Clerk, Nonlinear Interaction Effects in a Strongly Driven Optomechanical Cavity, *Physical Review Letters* **111**, 053602 (2013).

- [48] B. Hauer, J. Combes, and J. Teufel, Nonlinear Sideband Cooling to a Cat State of Motion, *Physical Review Letters* **130**, 213604 (2023).
- [49] M. Dykman, G. Rastelli, M. Roukes, and E. M. Weig, Resonantly Induced Friction and Frequency Combs in Driven Nanomechanical Systems, *Physical Review Letters* **122**, 254301 (2019).
- [50] M. R. Vanner, I. Pikovski, G. D. Cole, M. S. Kim, Č. Brukner, K. Hammerer, G. J. Milburn, and M. Aspelmeyer, Pulsed quantum optomechanics, *Proceedings of the National Academy of Sciences* **108**, 16182 (2011).
- [51] S. E. Nigg, H. Paik, B. Vlastakis, G. Kirchmair, S. Shankar, L. Frunzio, M. H. Devoret, R. J. Schoelkopf, and S. M. Girvin, Black-Box Superconducting Circuit Quantization, *Physical Review Letters* **108**, 240502 (2012).
- [52] D. I. Schuster, A. Wallraff, A. Blais, L. Frunzio, R.-S. Huang, J. Majer, S. M. Girvin, and R. J. Schoelkopf, ac Stark Shift and Dephasing of a Superconducting Qubit Strongly Coupled to a Cavity Field, *Physical Review Letters* **94**, 123602 (2005).

# Supplemental Material: Instabilities near ultrastrong coupling in microwave optomechanical cavity

Soumya Ranjan Das, Sourav Majumder, Sudhir Kumar Sahu, Ujjawal Singhal, Tanmoy Bera, and Vibhor Singh  
*Department of Physics, Indian Institute of Science, Bangalore-560012 (India)*

(Dated: August 21, 2023)

## I. DEVICE FABRICATION

The nanofabrication consists of several steps, which are described below. The details of the fabrication processes are schematically illustrated in the Fig. S1. We begin with a 2-inch diameter double-side polished sapphire wafer and dice it into smaller substrates of  $5 \times 8 \text{ mm}^2$  size. Aluminum parallel plate capacitors are then fabricated onto these substrates after cleaning.

**Step-1 Substrate cleaning:** These diced pieces are heated on a sample holder in PG remover for 30 minutes at  $80^\circ\text{C}$  and then rinsed with IPA. Samples are then dipped in concentrated  $\text{HNO}_3$  for 10 minutes and followed by rinsing with DI water. The samples are then cleaned in piranha solution for 10 minutes, followed by rinsing with DI water.

**Step-2 Patterning of the base electrode:** Cleaned wafer pieces are loaded in an electron beam evaporator, and then 60 nm thin film of aluminum is deposited with a deposition rate of  $3 \text{ \AA/s}$ . Subsequently, the samples are spin-coated with photoresist (S1813). We use a spin speed of 6000 RPM to minimize the edge bead. The resist-coated samples are baked at  $110^\circ\text{C}$  for 90 sec. The base electrode is patterned using a MJB4 lithography tool, followed by development in a 4:1 solution of water and developer AZ351B for 6-7 seconds. The exposed aluminum is etched with a 3:1 solution of  $\text{H}_3\text{PO}_4$  and  $\text{HNO}_3$  and rinsed with DI water. The samples are dipped in a 1:2 solution of MF26A and water for 10 seconds to remove the aluminum oxide layer, followed by rinsing with DI water. Removal of the photoresist is done in acetone for 5 minutes, followed by rinsing with IPA. Further, the samples are exposed to  $\text{O}_2$  plasma with 50 W power for 1 minute to remove any residue of photoresist.

**Step-3 Patterning of the sacrificial layer:** Silicon of 200 nm is deposited using a sputtering machine followed by spin coating with photoresist AZ5214E at 6000 RPM and followed by baking for 90 seconds at  $110^\circ\text{C}$ . Similar to previous steps, the sacrificial layer is patterned with MJB4 and developed in a 4:1 solution of water and AZ351B for 10-12 seconds. The exposed silicon is etched in a reactive ion etching machine with  $\text{SF}_6$  gas for 2 minutes, followed by photoresist removal in  $80^\circ\text{C}$  hot PG remover for 30 minutes. The sample is again exposed to  $\text{O}_2$  plasma with 50 W power for 2 minutes to remove any residue of photoresist.

**Step-4 Patterning of the top electrode:** A 100 nm thick aluminum film is deposited on the samples using the sputtering technique. Patterning of the top electrode follows the exact same procedure as the bottom electrode.

**Step-5 Etching of the sacrificial layer and release of the drum:** To avoid any electrostatic effect leading to the collapse of the drum, we shorted the two electrodes of the sample using a wire bond before the release process. The Si-sacrificial layer is etched using a high-pressure  $\text{SF}_6$  etch in a reactive ion system. The following are the typical RIE etch parameters: 50W RF power, 95 mTorr chamber pressure, 100 sccm flow rate of  $\text{SF}_6$ , seven cycles of 8 mins of etching process with 2 mins break between each cycle.

## II. MEASUREMENT SETUP

Fig. S2(a) shows the measurement set up for the optomechanically induced absorption technique. We use a red-detuned strong pump generated by a signal generator (R&S - SMF100A) and a probe tone near the cavity resonance frequency provided by a vector network analyser (R&S - ZNB20). The time base of both the signal generators are synchronized by an external 10 MHz clock. We use a directional coupler at the input to combine both signals. The input signal goes through a series of attenuators at different cooling stages in the dilution refrigerator before reaching the input of the cavity. The output from the cavity gets amplified by a HEMT amplifier at the 4 K stage before reaching the input of the vector network analyser.

Fig. S2(b) shows the time domain measurement setup used to perform the optomechanical swap. The pump is pulse-modulated using a trigger. The pulse-modulated pump output is then added to the probe signal. To maintain vector control over the probe signal, we use a home-built *IQ*-modulation-demodulation box based on *IQ*-mixer (Marki-IQ4509) for up-conversion, and a Mini-Circuits-ZMX-10G+ three-port mixer for down-conversion. The base-band signals for the probe are generated from the 2-channel outputs of a lock-in amplifier (Zurich instruments - UHFLI). The

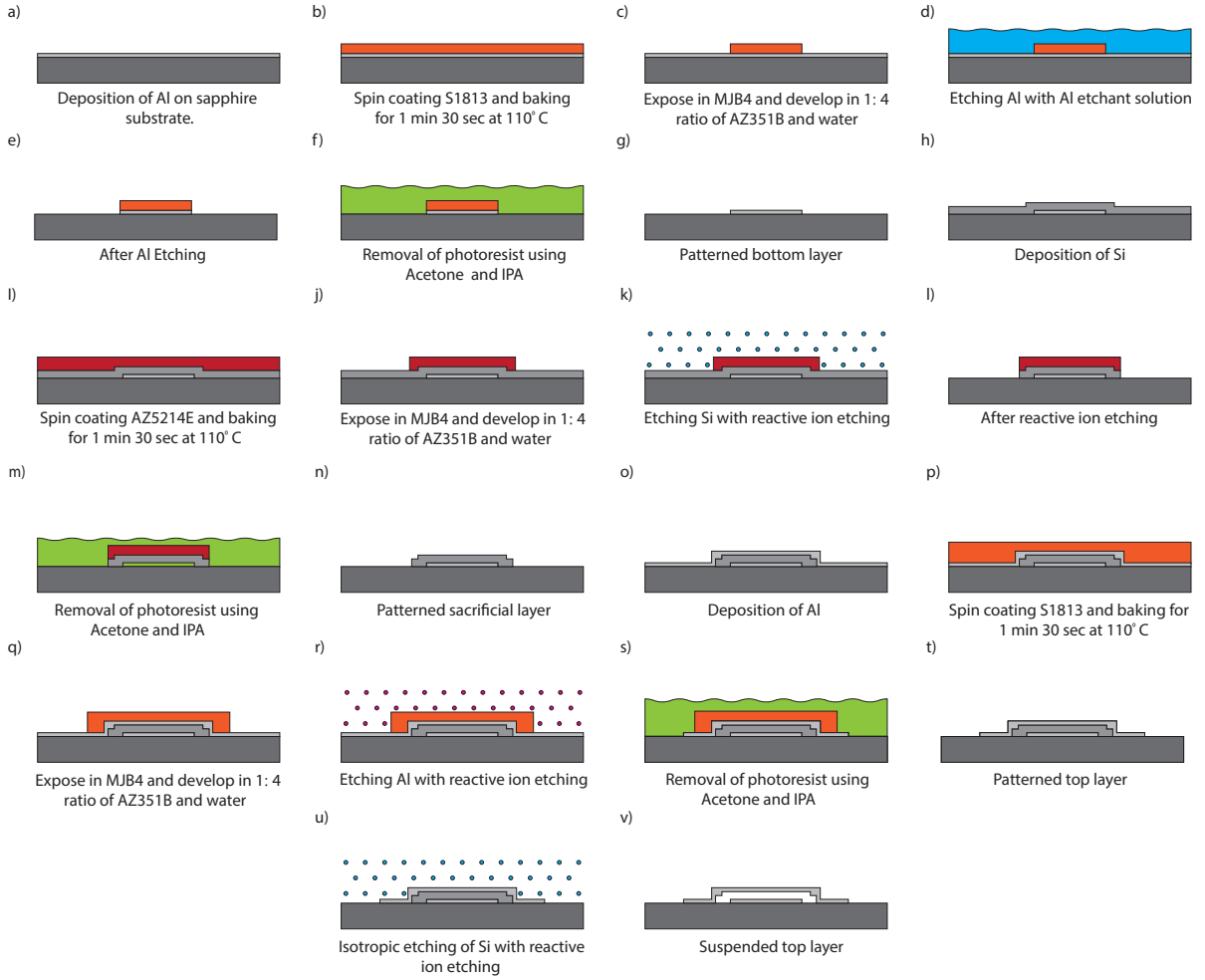


FIG. S1. A schematic of the fabrication process summarizing the key steps

TABLE S1. Important device parameters

Description	Parameter	Value	Unit
Cavity frequency	$\omega_e$	4.86	GHz
Microwave input coupling rate	$\kappa_{e1}$	90	kHz
Microwave output coupling rate	$\kappa_{e2}$	190	kHz
Cavity linewidth	$\kappa$	380	kHz
Mechanical frequency	$\omega_m$	6.32	MHz
Mechanical dissipation rate	$\gamma_m$	20	Hz
Single photon coupling rate	$g_0$	165	Hz

demodulated RF output from the demodulator box is sent to the lock-in amplifier's inputs to record the quadratures  $I(t)$  and  $Q(t)$ .

### III. KEY DEVICE PARAMETERS

Table S1 lists some key device parameters extracted from various experiments. Calibration of the external coupling rates of the microwave input and output ports ( $\kappa_{e1}$  and  $\kappa_{e2}$ ) is performed in a separate cooldown where we measured the reflection coefficients from both microwave ports using two separate HEMT amplifiers.

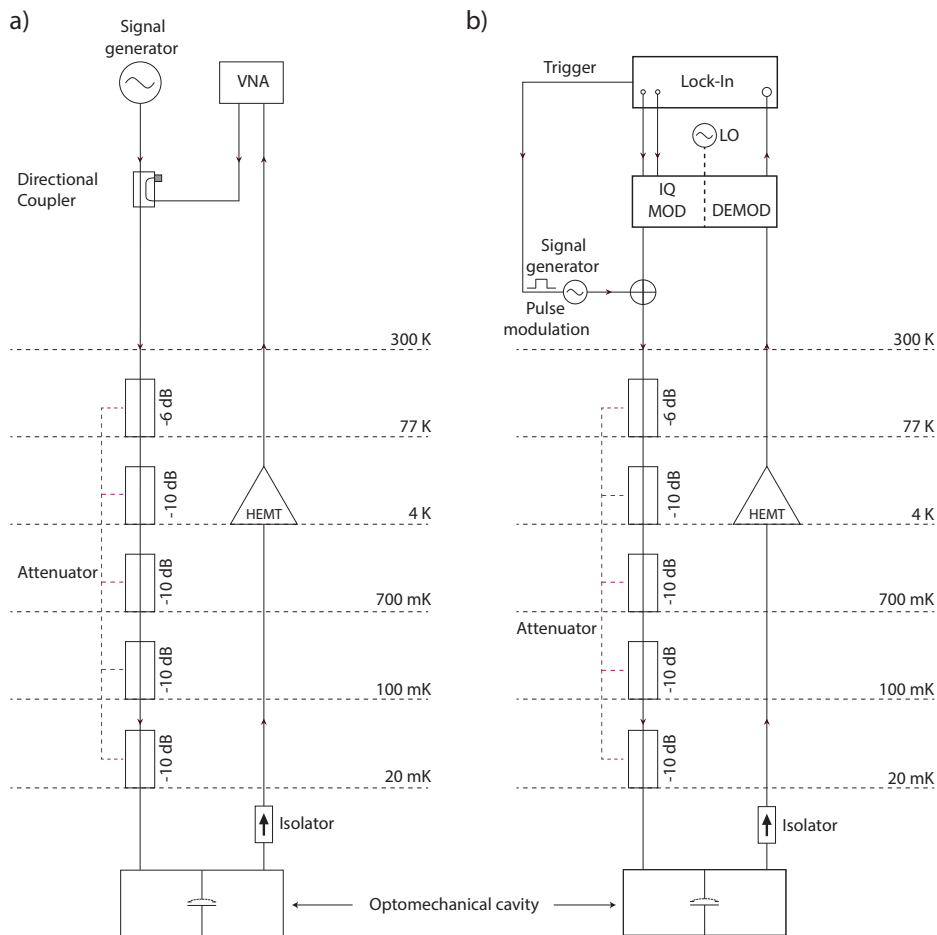


FIG. S2. Setup for (a) spectroscopy and (b) time-domain measurements.

#### IV. ESTIMATION OF SINGLE PHOTON COUPLING RATE $g_0$ USING SIMULATION

We perform electromagnetic simulations using COMSOL to estimate the single photon coupling strength  $g_0$ . We model a 3D cavity of dimensions  $26 \times 26 \times 6$  mm<sup>3</sup> and a sapphire chip placed at its center, as shown in Fig. S3(a). The sapphire chip has two electrodes on either side. The mechanically-compliant capacitor is modeled as a lumped port placed at the center, as shown by the red arrow in Fig. S3(b). We perform a frequency domain simulation by defining the Al surfaces as “perfect electric conductor” boundary condition, which then gives us the admittance response of the system for the defined frequency range. We then add the admittance contribution of the capacitor to the admittance response of the simulation in such a manner that the zero crossing in the imaginary part of the admittance curve matches with the experimentally observed resonance frequency of the cavity [1]. This gives us an estimate of the capacitance of the parallel plate capacitor. Thus, we can estimate the gap ( $d$ ) between the two plates using the lateral dimensions of the drum. The single photon coupling strength for an optomechanical device can be written as  $\eta\omega_c x_{zp}/2d$ , where  $\eta$  is the capacitance participation ratio of the mechanical capacitor to the total capacitance of the device,  $x_{zp}$  is the vacuum fluctuation of the mechanical resonator.

#### V. ESTIMATION OF ATTENUATION IN THE INPUT LINE, AND CALIBRATION OF $g_0$

The input line attenuation was determined in a separate cooldown using a measurement technique commonly employed in circuit-quantum electrodynamics (c-QED) systems to calculate the intra-cavity photon population. In this case, a transmon qubit of frequency  $\omega_q/2\pi = 3.6$  GHz was placed inside the 3D cavity. The frequency shift due to the ac-Stark shift of the transmon was measured to determine the mean cavity photon population [2]. The frequency

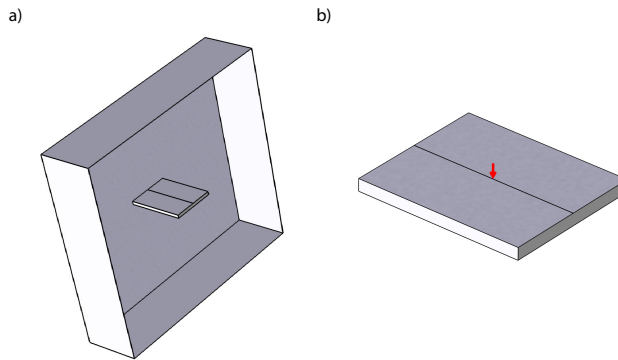


FIG. S3. (a) A snippet of the microwave design used in COMSOL showing the 3D cavity and the placement of the sapphire chip. (b) Sapphire chip with two electrodes. The position of the lumped port in place of the capacitor is pointed by the red arrow.

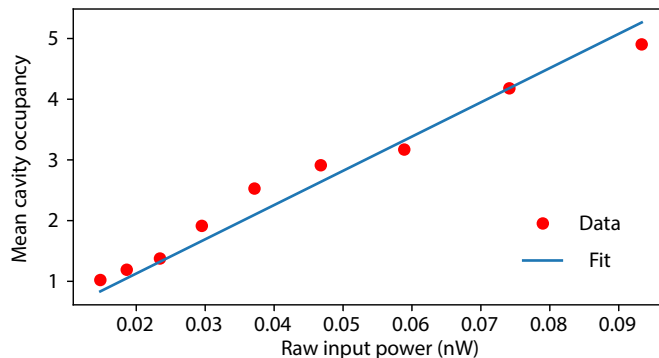


FIG. S4. The input line attenuation was calibrated by calculating the cavity photon population using the ac-Stark shift and plotting it against the input power at the cable. The fitted parameter was used to determine the line attenuation, which was found to be 53 dB.

of the transmon exhibits a linear relationship with the mean cavity photon population given by  $\tilde{\omega}_q = \omega_q + 2\chi\bar{n}$ , where  $\bar{n}$  is mean cavity occupation and  $\chi$  is the dispersive frequency shift. The dispersive shift can be expressed as  $\chi = J^2 \frac{\alpha}{\Delta(\Delta+\alpha)}$ , where  $\Delta = \omega_q - \omega_c$  is the detuning between the qubit and the cavity,  $\alpha$  is the qubit anharmonicity, and  $J$  is the coupling between the qubit and cavity. The qubit parameters such as  $J$  and anharmonicity  $\alpha$  can be independently measured using single-tone and two-tone spectroscopy methods. Thus, the calculated dispersive shift can be used to calibrate the cavity photon population, and hence the attenuation of the cables. For our device, we find the dispersive shift to be  $\chi/2\pi = -0.12$  MHz. Fig. S4 displays the cavity photon population as a function of input power at the cable external to the setup. By using the total attenuation of the input line as a fitting parameter, the attenuation was inferred to be 53 dB for the input line. Combined with the optomechanically induced absorption (OMIA) measurements, it further allows us to calibrate the single-photon optomechanical coupling rate to be  $2\pi \times 165$  Hz, which closely matches with the estimation made using COMSOL simulations.

## VI. ESTIMATION OF KERR-SHIFT DUE TO KINETIC INDUCTANCE

We perform cavity transmission measurements at different probe powers. With increased input probe power, the cavity shows a shift in the resonant frequency. We attribute the shift in the cavity frequency to the optomechanical Kerr effect and shift due to the kinetic inductance of aluminium film. After removing the optomechanical Kerr-shift per photon  $-2g_0^2/\omega_m$ , we attribute the rest of the Kerr-shift to the kinetic inductance of the superconducting film. We estimated it to be 5 mHz/photon at the highest probe powers used in the experiments.

## VII. CALCULATIONS OF THE CAVITY TRANSMISSION

The Hamiltonian for an optomechanical cavity system is given by

$$\tilde{\mathcal{H}} = \hbar\omega_c(\hat{x})(\hat{n} + 1/2) + \hbar\omega_m(b^\dagger b + 1/2), \quad (\text{S1})$$

where the operator  $b(b^\dagger)$  is the annihilation(creation) operator for the mechanical resonator, and  $\omega_c(\omega_m)$  represents the resonant frequency of the microwave cavity (mechanical resonator). The operator  $\hat{n}$  is the photon number operator for the microwave cavity. The resonant frequency of the microwave cavity depends on the gap between the capacitor plates. As the bottom plate is fixed, the microwave cavity's resonant frequency depends on the top plate's position (mechanical oscillator), which is freely suspended. When the amplitude of the mechanical oscillator is small, we can expand  $\omega_c(\hat{x}) \simeq \omega_c - g_0\hat{x}/x_{zp}$ , where  $x_{zp} = \sqrt{\hbar/2m\omega_m}$  is the vacuum fluctuations of the mechanical oscillator,  $g_0$  is the single photon coupling strength, and  $m$  is the mass of the mechanical resonator.

With a pump tone at  $\omega_d = \omega_c + \Delta$ , the cavity gets populated with  $n_d$  coherent microwave photons with the pump tone frequency. The number of photons inside the cavity after writing in terms of mean coherent amplitude  $\sqrt{n_d}$  and fluctuating term  $\hat{a}$  becomes

$$\hat{n} = (\sqrt{n_d}e^{i\omega_d t} + \hat{a}^\dagger)(\sqrt{n_d}e^{-i\omega_d t} + \hat{a}) = n_d + \sqrt{n_d}(\hat{a}^\dagger e^{-i\omega_d t} + \hat{a}e^{i\omega_d t}) + \hat{a}^\dagger \hat{a}. \quad (\text{S2})$$

Thus, the resultant Hamiltonian can be written as,

$$\begin{aligned} \tilde{\mathcal{H}} &= \hbar\omega_c n_d + \hbar\omega_c \hat{a}^\dagger \hat{a} + \hbar\omega_c \sqrt{n_d}(\hat{a}e^{i\omega_d t} + \hat{a}^\dagger e^{-i\omega_d t}) - \hbar g_0 n_d (\hat{b}^\dagger + \hat{b}) + \\ &\hbar g_0 (\hat{a}^\dagger e^{-i\omega_d t} + \hat{a}e^{i\omega_d t})(\hat{b}^\dagger + \hat{b}) + \frac{\hbar}{2} g_0 (\hat{b}^\dagger + \hat{b}) - \hbar g_0 (\hat{b}^\dagger + \hat{b}) \hat{a}^\dagger \hat{a} + \hbar\omega_m \hat{b}^\dagger \hat{b}. \end{aligned}$$

To get the equation of motion for the coupled system, we use the Heisenberg-Langevin approach to get

$$\dot{\hat{a}} = -\frac{\kappa}{2}\hat{a} + \sqrt{\kappa_{e1}}\hat{a}_{in} - i\omega_c\sqrt{n_d}e^{-i\omega_d t} + ig_0(\hat{b}^\dagger + \hat{b})\hat{a} + ig(\hat{b}^\dagger + \hat{b})e^{-i\omega_d t} - i\omega_c\hat{a}, \quad (\text{S3})$$

$$\dot{\hat{b}} = (-i\omega_m - \frac{\gamma_m}{2})\hat{b} + ig_0\hat{a}^\dagger\hat{a} + \sqrt{\gamma_m}\hat{b}_{in} + ig_0n_d + i\sqrt{n_d}g_0(\hat{a}e^{-i\omega_d t} + \hat{a}^\dagger e^{-i\omega_d t}), \quad (\text{S4})$$

where  $\kappa_{e1}$  is the external coupling rate of the cavity,  $\gamma$  is the mechanical dissipation rate, and  $\hat{a}_{in}(\hat{b}_{in})$  is the input noise operators for the microwave (mechanical) field.

Taking the Fourier transform of the equation of motions and putting them in a compact matrix form, we get

$$C(\omega) \begin{bmatrix} \hat{a}(\omega + \omega_d) \\ \hat{b}(\omega) \\ \hat{a}^\dagger(\omega_d - \omega) \\ \hat{b}^\dagger(-\omega) \end{bmatrix} + \begin{bmatrix} -\omega_c\sqrt{n_d}\delta(\omega) \\ g_0n_d\delta(\omega) \\ \omega_c\sqrt{n_d}\delta(\omega) \\ -g_0n_d\delta(\omega) \end{bmatrix} = \begin{bmatrix} i\sqrt{\kappa_{e1}}\hat{a}_{in}(\omega + \omega_d) \\ i\sqrt{\gamma_m}\hat{b}_{in}(\omega) \\ i\sqrt{\kappa_{e1}}\hat{a}_{in}^\dagger(\omega_d - \omega) \\ i\sqrt{\gamma_m}\hat{b}_{in}^\dagger(-\omega) \end{bmatrix}. \quad (\text{S5})$$

The mode-coupling matrix  $C(\omega)$  is given by

$$C(\omega) = \begin{bmatrix} \chi_a^{-1}(\omega + \omega_d) & g & 0 & g \\ g & \chi_b^{-1}(\omega) & g & 0 \\ 0 & -g & -\chi_a^{-1}(\omega_d - \omega)^* & -g \\ -g & 0 & -g & -\chi_b^{-1}(-\omega)^* \end{bmatrix}, \quad (\text{S6})$$

where

$$\chi_a(\omega) = 1/(\omega - \omega_c + i\kappa/2), \quad (\text{S7})$$

$$\chi_b(\omega) = 1/(\omega - \omega_m + i\gamma_m/2) \quad (\text{S8})$$

are the complex susceptibility functions for the cavity and mechanical mode, respectively.

We use optomechanically induced absorption (OMIA) to couple the cavity and mechanical motion and get the resultant response of the dressed mode. Here, we provide a strong red-detuned pump at a frequency  $\omega_c - \omega_m$  and a weak probe tone near cavity resonance frequency,  $\omega_c$ . The resultant transmission through the cavity at a frequency  $\omega$  is then given by

$$T(\omega) = i\sqrt{\kappa_{e1}\kappa_{e2}}\chi_a^{eff}(\omega), \quad (\text{S9})$$

where  $\chi_a^{eff}(\omega)$  is given by  $(C^{-1}(\omega))_{11}$ ,  $\kappa_{e1}(\kappa_{e2})$  is the input(output) coupling rate.

### VIII. LINEAR STABILITY TEST (ROUTH-HURWITZ STABILITY CRITERIA)

To understand the instabilities at large pump powers, we consider the optomechanical Kerr-nonlinearity and the kinetic inductance of aluminium film. We start with the full optomechanical Hamiltonian in the rotating frame of the pump frequency. It can be written as,

$$\mathcal{H} = -\Delta \hat{a}^\dagger \hat{a} - \frac{\alpha_c}{2} \hat{a}^\dagger \hat{a}^\dagger \hat{a} \hat{a} + \omega_m \hat{b}^\dagger \hat{b} - g_0 \hat{a}^\dagger \hat{a} (\hat{b} + \hat{b}^\dagger) + iE (\hat{a} + \hat{a}^\dagger), \quad (\text{S10})$$

where  $\alpha_c$  is the Kerr-coefficient to model the kinetic inductance. Using the Heisenberg-Langevin approach and the semi-classical approximation, the equations of motions can be written as,

$$\dot{\alpha} = (i\Delta - \frac{\kappa}{2})\alpha + i\alpha_c |\alpha|^2 \alpha + ig_0 \alpha (\beta + \beta^*) + E, \quad (\text{S11})$$

$$\dot{\beta} = -(i\omega_m + \frac{\gamma_m}{2})\beta + ig_0 |\alpha|^2, \quad (\text{S12})$$

where  $E = \sqrt{\kappa_{e1}} \hat{a}_{in}$ ,  $\alpha = \langle \hat{a} \rangle$  and  $\beta = \langle \hat{b} \rangle$ . By representing  $\alpha$  and  $\beta$  in the complex form, we get

$$\alpha = x + iy, \quad (\text{S13})$$

$$\beta = p + iq. \quad (\text{S14})$$

Therefore,

$$\dot{x} = f_1(x, y, p, q) = -\frac{\kappa}{2}x - \Delta y - 2g_0 p y - \alpha_c y (x^2 + y^2) + E, \quad (\text{S15})$$

$$\dot{y} = f_2(x, y, p, q) = \Delta x - \frac{\kappa}{2}y + 2g_0 p x + \alpha_c x (x^2 + y^2), \quad (\text{S16})$$

$$\dot{p} = f_3(x, y, p, q) = -\frac{\gamma_m}{2}p + \omega_m q, \quad (\text{S17})$$

$$\dot{q} = f_4(x, y, p, q) = g_0 x^2 + g_0 y^2 - \omega_m p - \frac{\gamma_m}{2}q. \quad (\text{S18})$$

Following the approach used in Ref. [3, 4], we obtain the fixed points of the system by setting the first derivative of the real and imaginary parts of both  $\alpha$  and  $\beta$  to zero, *i.e.*  $\dot{x} = \dot{y} = \dot{p} = \dot{q} = 0$ . Combining Eq. S15 and Eq. S16 and representing  $x, y, q$  in terms of  $p$ , we get

$$x = \frac{\kappa}{2} \frac{E}{A^2 + (\frac{\kappa}{2})^2}, \quad (\text{S19})$$

$$y = \frac{A E}{A^2 + (\frac{\kappa}{2})^2}, \quad (\text{S20})$$

$$q = \frac{\gamma_m}{2\omega_m} p, \quad (\text{S21})$$

where

$$A = \Delta + B p \quad (\text{S22})$$

and

$$B = \left[ 2g_0 + \frac{\alpha_c}{g_0} \left( \omega_m + \frac{\gamma_m^2}{4\omega_m} \right) \right]. \quad (\text{S23})$$

Substituting the above calculated values of  $x, y, q$  in Eq. S18, we get a cubic polynomial equation,

$$B^2 \left( \omega_m + \frac{\gamma_m^2}{4\omega_m} \right) p^3 + 2B\Delta \left( \omega_m + \frac{\gamma_m^2}{4\omega_m} \right) p^2 + \left( \Delta^2 + \frac{\kappa^2}{4} \right) \left( \omega_m + \frac{\gamma_m^2}{4\omega_m} \right) p - g_0 E^2 = 0. \quad (\text{S24})$$

The roots of the polynomial will give the fixed point solutions for  $x, y, q$ . Considering the roots to be  $(\bar{x}, \bar{y}, \bar{p}, \bar{q})$ , the nature of the fixed points can be understood by considering the time evolution of a small perturbation around these points. We define a small perturbation around the fixed points as  $Z_i = k_i - \bar{k}_i$ , where  $i = 1, 2, 3, 4$  corresponding to  $(k_1, k_2, k_3, k_4) \equiv (x, y, p, q)$ .

To obtain the time evolution of  $Z_i$ , we solve  $\dot{Z}_i = \dot{k}_i = f_i(x, y, p, q)$  by expanding the  $f_i$  polynomials around the fixed point and retaining the first-order terms as shown below:

$$f_j(x, y, p, q) \approx f_j \Big|_{x,y,p,q=\bar{x},\bar{y},\bar{p},\bar{q}} + \sum_{k=x,y,p,q} (k_i - \bar{k}_i) \frac{\partial f_j}{\partial k_i} \Big|_{x,y,p,q=\bar{x},\bar{y},\bar{p},\bar{q}}. \quad (\text{S25})$$

This allows us to obtain the four coupled equations of motion for the small perturbations around fixed points as,

$$\frac{d}{dt} \begin{bmatrix} Z_1 \\ Z_2 \\ Z_3 \\ Z_4 \end{bmatrix} = \begin{bmatrix} \frac{\partial f_1}{\partial x} & \frac{\partial f_1}{\partial y} & \frac{\partial f_1}{\partial p} & \frac{\partial f_1}{\partial q} \\ \frac{\partial f_2}{\partial x} & \frac{\partial f_2}{\partial y} & \frac{\partial f_2}{\partial p} & \frac{\partial f_2}{\partial q} \\ \frac{\partial f_3}{\partial x} & \frac{\partial f_3}{\partial y} & \frac{\partial f_3}{\partial p} & \frac{\partial f_3}{\partial q} \\ \frac{\partial f_4}{\partial x} & \frac{\partial f_4}{\partial y} & \frac{\partial f_4}{\partial p} & \frac{\partial f_4}{\partial q} \end{bmatrix} \begin{bmatrix} Z_1 \\ Z_2 \\ Z_3 \\ Z_4 \end{bmatrix}. \quad (\text{S26})$$

Upon substituting the values of  $f_i$ 's, and evaluating the derivative at the fixed points, we get

$$\frac{d}{dt} \begin{bmatrix} Z_1 \\ Z_2 \\ Z_3 \\ Z_4 \end{bmatrix} = S \begin{bmatrix} Z_1 \\ Z_2 \\ Z_3 \\ Z_4 \end{bmatrix}, \quad (\text{S27})$$

where the evolution matrix  $S$  is given by

$$S = \begin{bmatrix} -\frac{\kappa}{2} - 2\alpha_c \bar{x}\bar{y} & -\Delta - 2g_0\bar{p} - \alpha_c \bar{x}^2 - 3\alpha_c \bar{y}^2 & -2g_0\bar{y} & 0 \\ \Delta + 2g_0\bar{p} + 3\alpha_c \bar{x}^2 + \alpha_c \bar{y}^2 & -\frac{\kappa}{2} + 2\alpha_c \bar{x}\bar{y} & 2g_0\bar{x} & 0 \\ 0 & 0 & -\frac{\gamma_m}{2} & \omega_m \\ 2g_0\bar{x} & 2g_0\bar{y} & -\omega_m & -\frac{\gamma_m}{2} \end{bmatrix} \quad (\text{S28})$$

The solution of the matrix equation will have the following form,

$$Z(t) = \sum_{i=1}^4 c_i W_i \exp \lambda_i t, \quad (\text{S29})$$

where  $c_i$ 's are the constants of integration,  $W_i$ 's and  $\lambda_i$ ' are the eigenvectors and eigenvalues of the matrix  $S$ .

From Eq. S29, it is evident that stable solutions are only possible iff all the eigenvalues have a negative real part. To cross-check the results from the nonlinear optomechanically coupling can be obtained in a straightforward manner by setting  $\alpha_c$  to zero, as given by,

$$\frac{d}{dt} \begin{bmatrix} Z_1 \\ Z_2 \\ Z_3 \\ Z_4 \end{bmatrix} = \begin{bmatrix} -\frac{\kappa}{2} & -\Delta - 2g_0\bar{p} & -2g_0\bar{y} & 0 \\ \Delta + 2g_0\bar{p} & -\frac{\kappa}{2} & 2g_0\bar{x} & 0 \\ 0 & 0 & -\frac{\gamma_m}{2} & \omega_m \\ 2g_0\bar{x} & 2g_0\bar{y} & -\omega_m & -\frac{\gamma_m}{2} \end{bmatrix} \begin{bmatrix} Z_1 \\ Z_2 \\ Z_3 \\ Z_4 \end{bmatrix}. \quad (\text{S30})$$

Instability boundaries obtained from the above formalism by choosing  $\alpha_c/2\pi = 0, 5, 12.5$  mHz/photo are included in Fig. 4(b) of the main text.

## IX. MEASUREMENT OF INSTABILITY BOUNDARY

The measurement of the instability boundary is performed in two ways. In the first method, we send a pump signal and measure the power spectral density (PSD) of the output signal near the pump frequency. The pump

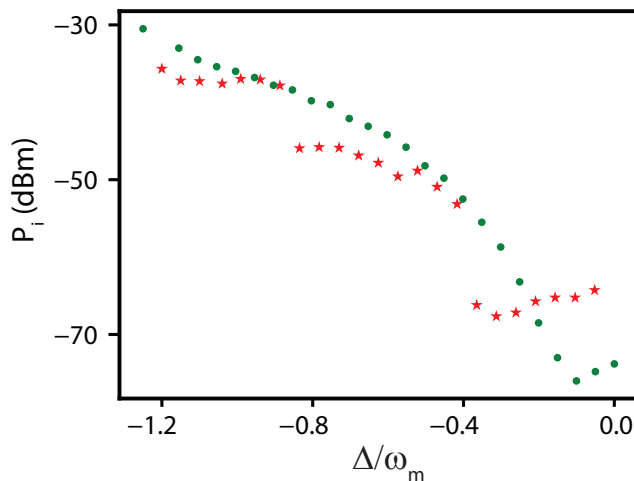


FIG. S5. The green dots represent the measured instability boundary when the pump power is swept upwards. The red stars represent the instability boundary obtained while sweeping the pump power downwards.

power is manually changed while sweeping it upwards and the threshold power at the onset of instability is recorded. Subsequently, the power is reduced to the start value, and the measurement for the next detuning is carried out in the same way. In the second method, we divide the parameter space spanned by  $\Delta$  and  $P_i$  into a regular grid. The resolution of drive frequency and pump power is 300 kHz and 0.1 dBm respectively. We use an automated data recording which records the power spectral density for different parameter values on the grid. The instability boundary, period-doubling/tripling and chaos are then extracted by analyzing the records of PSD. We do not see any substantial difference in the manual and automated datasets. We, however observe a hysteresis when the pump power is swept upwards or downwards as shown in Fig. S5. We suspect that this hysteresis might come from the heating of the device or from the duffing behavior of the mechanical resonator.

## X. FROM OPTOMECHANICALLY-INDUCED ABSORPTION TO THE ULTRA-STRONG COUPLING

To characterize the ultrastrong coupling limit, we start with a weak pump signal at the red sideband. We gradually increase the pump power as we move from the weak coupling limit to the strong coupling limit. At high pump powers, the pump frequency is adjusted as the cavity resonance frequency shifts down due to the static Kerr-shift. Fig. S6 shows the transmission spectra of the cavity at different pump photons.

## XI. THEORETICAL MODEL AND MEASUREMENT OF OMIA IN THE TIME DOMAIN

To theoretically model the observed behavior of Fig. 3(d) in the main text, we start with the Hamiltonian in a rotating frame at the drive frequency as given by S10. By including the probe part, the total Hamiltonian can be written as,

$$\mathcal{H} \approx -\tilde{\Delta}\hat{a}^\dagger\hat{a} + \omega_m\hat{b}^\dagger\hat{b} + g(\hat{a} + \hat{a}^\dagger)(\hat{b} + \hat{b}^\dagger) + S_p(\hat{a}e^{i\Omega t} + \hat{a}^\dagger e^{-i\Omega t}), \quad (\text{S31})$$

where  $\tilde{\Delta} = \Delta + \frac{2g_0^2\alpha^2}{\omega_m}$ ,  $g = g_0\alpha$  and  $\Omega = \omega_p - \omega_d$ . From the equation above, we can obtain the following equation of motions (EOMs):

$$\langle \dot{\hat{a}} \rangle = (i\tilde{\Delta} - \frac{\kappa}{2})\langle \hat{a} \rangle + (-ig)\langle \hat{b} \rangle + (-ig)\langle \hat{b}^\dagger \rangle + S^*(t), \quad (\text{S32a})$$

$$\langle \dot{\hat{a}^\dagger} \rangle = (-i\tilde{\Delta} - \frac{\kappa}{2})\langle \hat{a}^\dagger \rangle + (ig)\langle \hat{b} \rangle + (ig)\langle \hat{b}^\dagger \rangle + S(t), \quad (\text{S32b})$$

$$\langle \dot{\hat{b}} \rangle = (-ig)\langle \hat{a} \rangle + (-ig)\langle \hat{a}^\dagger \rangle + (-i\omega_m - \frac{\gamma}{2})\langle \hat{b} \rangle, \quad (\text{S32c})$$

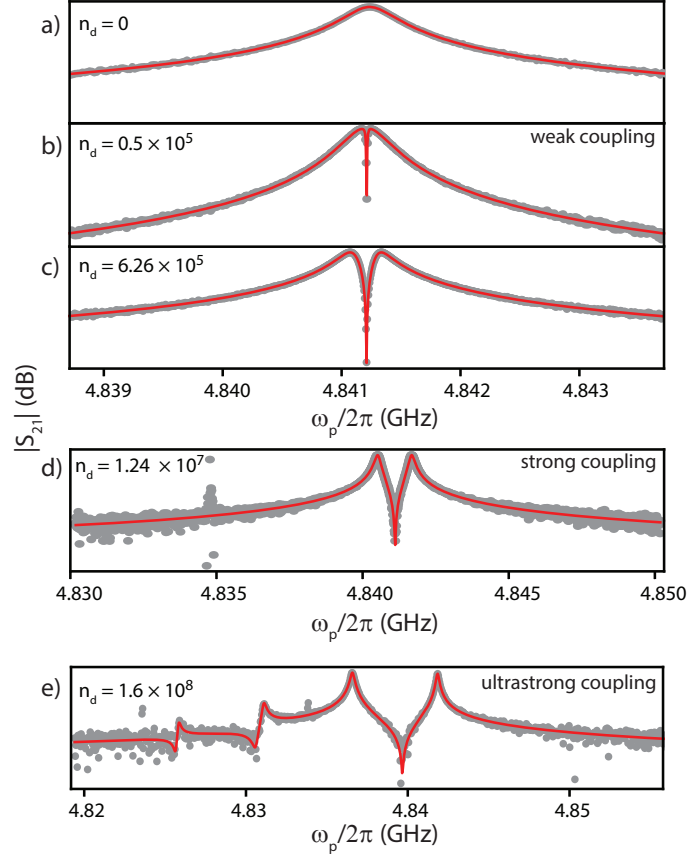


FIG. S6. (a) shows the cavity transmission  $|S_{21}|$  at the base temperature without any pump. (b)-(e) shows the OMIA measurement as pump strength is increased. The gray circles represent the measurement data, and the red curve represents the theoretical fit.

$$\langle \hat{b}^\dagger \rangle = (ig)\langle \hat{a} \rangle + (ig)\langle \hat{a}^\dagger \rangle + (i\omega_m - \frac{\gamma}{2})\langle \hat{b}^\dagger \rangle, \quad (\text{S32d})$$

where  $S(t) = iS_p e^{i\Omega t}$ . Similar to the approach described earlier, these coupled equations can be solved in the frequency domain. The solution obtained can then be transformed back to the time-domain using the inverse Fourier transform.

The solution of the EOM in the frequency domain can be written in a compact form as,

$$X[\omega] = \mathcal{B}(\omega) r[\omega], \quad (\text{S33})$$

where

$$\mathcal{B}(\omega) = \begin{bmatrix} -i\omega - i\tilde{\Delta} + \frac{\kappa}{2} & 0 & ig & ig \\ 0 & -i\omega + i\tilde{\Delta} + \frac{\kappa}{2} & -ig & -ig \\ ig & ig & -i\omega + i\omega_m + \frac{\gamma}{2} & 0 \\ -ig & -ig & 0 & -i\omega - i\omega_m + \frac{\gamma}{2} \end{bmatrix}^{-1}, \quad (\text{S34})$$

$$X(\omega) = \begin{bmatrix} \langle \hat{a} \rangle(\omega) \\ \langle \hat{a}^\dagger \rangle(\omega) \\ \langle \hat{b} \rangle(\omega) \\ \langle \hat{b}^\dagger \rangle(\omega) \end{bmatrix}, \quad \text{and} \quad r(\omega) = \begin{bmatrix} -2\pi i S_p \delta(\omega - \Omega) \\ 2\pi i S_p \delta(\omega + \Omega) \\ 0 \\ 0 \end{bmatrix}. \quad (\text{S35})$$

After performing the inverse Fourier transformation on the eq. S33, we can write the total solution as,

$$\begin{bmatrix} \langle \hat{a} \rangle(t) \\ \langle \hat{a}^\dagger \rangle(t) \\ \langle \hat{b} \rangle(t) \\ \langle \hat{b}^\dagger \rangle(t) \end{bmatrix} = [X_1 \ X_2 \ X_3 \ X_4] \begin{bmatrix} a_1 e^{\lambda_1 t} \\ a_2 e^{\lambda_2 t} \\ a_3 e^{\lambda_3 t} \\ a_4 e^{\lambda_4 t} \end{bmatrix} + iS_p \begin{bmatrix} -\mathcal{B}_{11}(\Omega)e^{-i\Omega t} + \mathcal{B}_{12}(-\Omega)e^{i\Omega t} \\ -\mathcal{B}_{21}(\Omega)e^{-i\Omega t} + \mathcal{B}_{22}(-\Omega)e^{i\Omega t} \\ -\mathcal{B}_{31}(\Omega)e^{-i\Omega t} + \mathcal{B}_{32}(-\Omega)e^{i\Omega t} \\ -\mathcal{B}_{41}(\Omega)e^{-i\Omega t} + \mathcal{B}_{42}(-\Omega)e^{i\Omega t} \end{bmatrix} \quad (\text{S36})$$

Here, the  $a_i$ 's are integration constants. The  $\lambda_i$ 's and  $X_i$ 's are eigenvalues and eigenvectors of the matrix  $M$  defined as,

$$M = \begin{bmatrix} i\tilde{\Delta} - \frac{\kappa}{2} & 0 & -ig & -ig \\ 0 & -i\tilde{\Delta} - \frac{\kappa}{2} & ig & ig \\ -ig & -ig & -i\omega_m - \frac{\gamma}{2} & 0 \\ ig & ig & 0 & i\omega_m - \frac{\gamma}{2} \end{bmatrix}. \quad (\text{S37})$$

If the initial boundary condition is defined at some point in time  $t_0$ , then the integration constant can be calculated as,

$$\begin{bmatrix} a_1 e^{\lambda_1 t_0} \\ a_2 e^{\lambda_2 t_0} \\ a_3 e^{\lambda_3 t_0} \\ a_4 e^{\lambda_4 t_0} \end{bmatrix} = [X_1 \ X_2 \ X_3 \ X_4]^{-1} \begin{bmatrix} \langle \hat{a} \rangle(t_0) + iS_p \mathcal{B}_{11}(\Omega)e^{-i\Omega t_0} - iS_p \mathcal{B}_{12}(-\Omega)e^{i\Omega t_0} \\ \langle \hat{a}^\dagger \rangle(t_0) + iS_p \mathcal{B}_{21}(\Omega)e^{-i\Omega t_0} - iS_p \mathcal{B}_{22}(-\Omega)e^{i\Omega t_0} \\ \langle \hat{b} \rangle(t_0) + iS_p \mathcal{B}_{31}(\Omega)e^{-i\Omega t_0} - iS_p \mathcal{B}_{32}(-\Omega)e^{i\Omega t_0} \\ \langle \hat{b}^\dagger \rangle(t_0) + iS_p \mathcal{B}_{41}(\Omega)e^{-i\Omega t_0} - iS_p \mathcal{B}_{42}(-\Omega)e^{i\Omega t_0} \end{bmatrix} \quad (\text{S38})$$

Since this solution is obtained in a frame rotating at the pump frequency, to obtain the solution at the probe frequency we shift the frame by  $\Omega$ , and neglect the terms rotating at  $2\Omega$ . The solution described above are plotted in Fig. S7(b,d). We emphasize here that the homogeneous solution containing  $e^{\lambda t}$  terms is responsible for the fringing pattern when the pump is turned on. The in-homogeneous solution gives the steady-state solution.

For measurement of the optomechanically-induced absorption in the time-domain, we send a weak probe signal near the cavity resonant frequency and a pulsed pump signal of duration  $\approx 15 \mu\text{s}$  near the red sideband of the cavity. The frequency of the probe signal is swept across the cavity frequency and the time domain response for each probe frequency is recorded. Fig. S7(a) shows the measurement of the imaginary part of the probe signal from the cavity. Panel (b) shows the plot of the solution from the theoretical calculations as described above, which show a quite decent match between experimental and theoretical results.

We would like to emphasize the technical challenge of such measurements. In order to capture the oscillatory nature of the transient solution, one must demodulate the microwave signal using a sufficiently large demodulation bandwidth (small time constant) of the lock-in amplifier. At the same time, the large demodulation bandwidth must not capture the pump signal which leaks through the cavity. Since the oscillation frequency of the transient solution is order  $2g$ , and pump-probe detuning is order  $\omega_m$ , it makes such measurements technically difficult as  $2g$  approaches  $\omega_m$ . Such measurement artifacts are more evident if we plot the magnitude ( $R$ ) of the probe signal, as shown in Fig. S7(c). The large value of magnitude below  $\Omega/2\pi = -2 \text{ MHz}$  for  $0 \leq t \leq 15 \mu\text{s}$ , is due to the pump signal falling into the demodulator bandwidth. In addition, this pump leakage also plagues the measurement when the pump is either turned on or turned off. At the switching event, the pump signal spreads in the frequency domain and spills into the bandwidth of the demodulator. It results in an ‘‘excess’’ value in  $R$ , which decays over a time-scale set by the cavity-dissipation rate and the demodulator bandwidth. Results of the magnitude calculations are shown in Fig. S7(d).

## XII. ZOOMED-IN PLOT OF PARAMETRIC INSTABILITY

Fig. S8 shows the detailed view of the parametric instability region showing the regions of period-doubling, period-tripling, and chaotic behaviors.

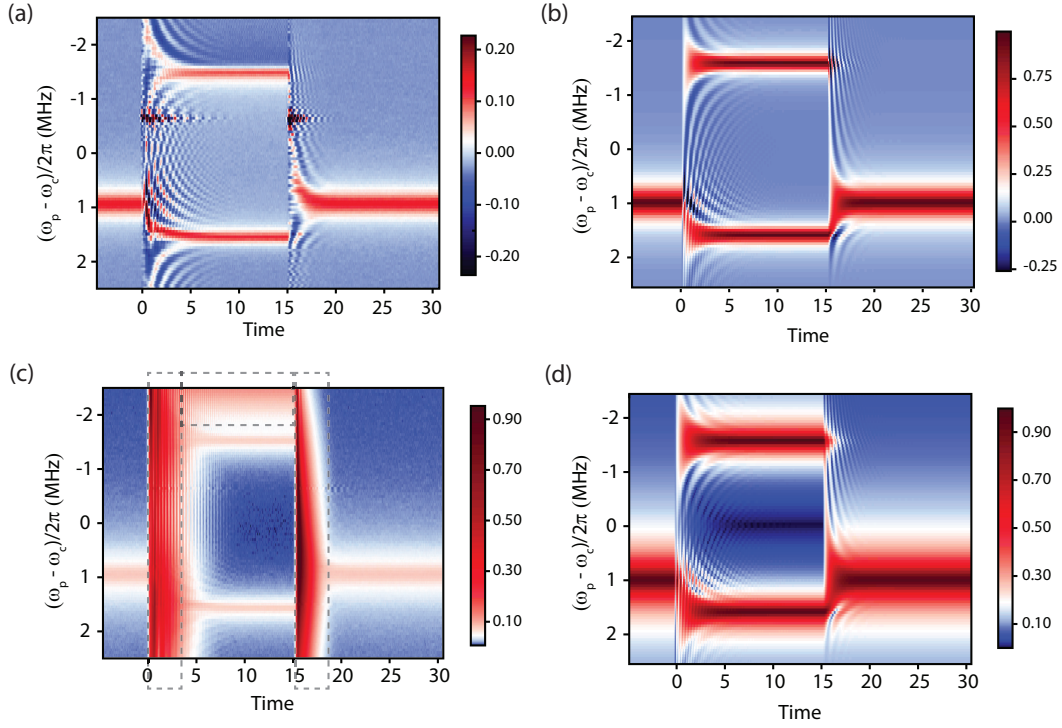


FIG. S7. (a) shows the measurement of the imaginary part of the probe signal. (b) shows the corresponding results from the theoretical calculations. (c) shows the measurement of the absolute value of the probe signal. The dotted box shows the presence of an excess offset signal coming from the pulsed pump signal captured by the lock-in demodulator. (d) show the theoretical calculations results for the magnitude of probe signal.

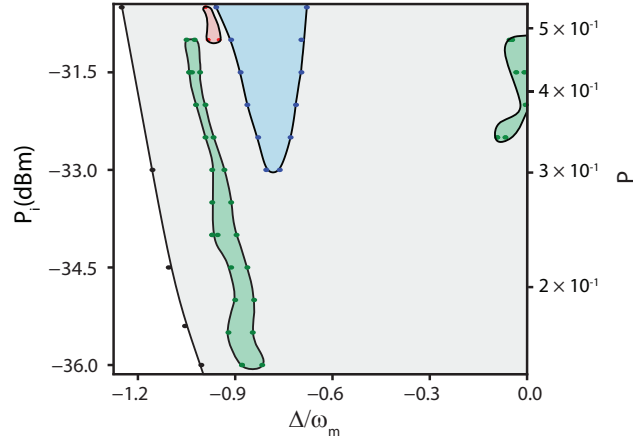


FIG. S8. Zoomed-in plot of Fig.4(b) of the main text.

- 
- [1] S. E. Nigg, H. Paik, B. Vlastakis, G. Kirchmair, S. Shankar, L. Frunzio, M. H. Devoret, R. J. Schoelkopf, and S. M. Girvin, Black-Box Superconducting Circuit Quantization, *Physical Review Letters* **108**, 240502 (2012).
  - [2] D. I. Schuster, A. Wallraff, A. Blais, L. Frunzio, R.-S. Huang, J. Majer, S. M. Girvin, and R. J. Schoelkopf, ac Stark Shift and Dephasing of a Superconducting Qubit Strongly Coupled to a Cavity Field, *Physical Review Letters* **94**, 123602 (2005).
  - [3] L. Bakemeier, A. Alvermann, and H. Fehske, Route to Chaos in Optomechanics, *Physical Review Letters* **114**, 013601 (2015).

- [4] T. F. Roque, F. Marquardt, and O. M. Yevtushenko, Nonlinear dynamics of weakly dissipative optomechanical systems, *New Journal of Physics* **22**, 013049 (2020).